Switchable optical and acoustic resolution photoacoustic dermoscope dedicated into *in vivo* biopsy-like of human skin

Haigang Ma (iD), Zhongwen Cheng, Zhiyang Wang, Wuyu Zhang, and Sihua Yang (iD)

View Online   Export Citation   CrossMark

Switchable optical and acoustic resolution photoacoustic dermoscope dedicated into *in vivo* biopsy-like of human skin

Haigang Ma,[1,2] (iD) Zhongwen Cheng,[2] Zhiyang Wang,[2] Wuyu Zhang,[2] and Sihua Yang[1,2,a)] (iD)

AFFILIATIONS

[1]MOE Key Laboratory of Laser Life Science and Institute of Laser Life Science, South China Normal University,
 Guangzhou 510631, China
[2]Guangdong Provincial Key Laboratory of Laser Life Science, College of Biophotonics, South China Normal University,
 Guangzhou 510631, China

[a)]yangsh@scnu.edu.cn

ABSTRACT

As a promising branch of optical absorption-based photoacoustic microscopy, photoacoustic dermoscopy (PAD) can provide manifold morphologic and functional information in clinical diagnosis and the assessment of dermatological conditions. However, most PAD setups are insufficient for clinical dermatology, given their single optical resolution (OR) or acoustic resolution (AR) mode, which results in poor spatiotemporal resolution or imaging depth for visualizing the internal texture of skin. Here, a switchable optical and acoustic resolution photoacoustic dermoscope (S-OR-ARPAD) system is developed, which provides a smooth transition from OR mode in microscopic imaging of superficial skin layers to AR mode when imaging at greater depths within intensely scattering deep skin layers. The lateral resolution can be seamlessly switched between 4.4 and 47 μm as the maximum imaging depth is switched between 1.2 and 1.8 mm for skin imaging. Using the S-OR-ARPAD, we identified the two distinct resolution modes responsible for resolving features of different skin layers and demonstrated the fine structures with strong contrast in the stratum corneum, dermal papillae, and microvascular structures in the horizontal plexus by imaging the healthy human skin at different locations.

*Published under license by AIP Publishing.* https://doi.org/10.1063/1.5143155

The hybrid nature of photoacoustic (PA) imaging, which depends on the detection of acoustic waves generated by the absorption of the laser with nanosecond pulses, has been successfully applied to *in vivo* imaging at scales from organelles to organs.[1–8] In particular, photoacoustic dermoscopy (PAD) emerges as a promising branch of photoacoustic microscopy (PAM), which takes advantage of the focusing abilities of either light [optical resolution (OR) PAD][9–15] or ultrasound [acoustic resolution (AR) PAD][16–22] to obtain high resolution PA images of optical contrast in biological tissues. Intuitively, the excitation light can generally be focused much more tightly than acoustic waves owing to its shorter wavelength range. Nevertheless, because of the diffraction, the focusing of light generally only stays possible within the ballistic regime of optical propagation in scattering media. Therefore, the focusing of light is generally limited to penetration depths no more than 1 mm in human skin tissue[23,24] in the optical resolution (OR) PAD (OR-PAD). Although the diffuse light in deep skin tissue can be effectively focused by some methods such as

time reversal processing,[25,26] in the common OR-PAD, longer photon paths increase the chance of tissue absorption, so that diffuse photons are too few to be practically useful beyond the soft-depth limit in human skin.[27–30] Similar to purely optical microscopy techniques, the OR-PAD eventually experiences severe limitations in terms of imaging depth due to the intense scattering of light in deep skin tissue.[2,3,31,32]

From the perspective of ultrasound, most acoustic resolution (AR) PAD (AR-PAD) designs tend to use a high frequency spherically focused ultrasonic detector with a single ultrasound detection element and a high numerical aperture.[17,33] With this approach, the imaging resolution of AR-PAD ranging from millimeter to less than a hundred micrometers can be obtained at deeper imaging depths than the ballistic range of optical propagation in scattering skin tissue, which is purely determined by the detecting characteristics and acoustic propagation.[2,3,33] Furthermore, the lateral resolution can be evaluated by the focal spot size of the detector, and the axial resolution is affected by both the bandwidth of the detector and the ultrasonic dispersion,

which generally increases with frequency in skin tissue.[34] Nevertheless, when efforts are made to increase the imaging resolution of AR-PAD by using extremely high numerical aperture detectors, the generation of PA signals is only efficiently detected in the sensitive area of the detector (focal zone) owing to the confinement of the suboptimal illuminating light, which results in difficult compromises between the achievable imaging resolution and the penetration depth for visualizing the internal texture of skin.[35,36] As of now, the PAM systems with hybrid optical and acoustic resolution have been developed by other teams,[37–42] but the imaging systems are rarely dedicated to the near-histological imaging of skin delamination and microstructures and qualitative evaluation of the melanin concentration and microvessel quantity in pre-clinical or in clinical practice (supplementary material, Table 1). Here, we proposed a switchable optical and acoustic resolution photoacoustic dermoscope (S-OR-ARPAD) with a custom made adjustable opto-sonovision objective appropriate for improving the dermoscopic depth and resolution range, in which case the S-OR-ARPAD could achieve high lateral resolution at superficial skin tissue layers in OR mode, whereas it could obtain moderate lateral resolution for deep skin tissue layer imaging in AR mode.

As shown in Fig. 1(a), the S-OR-ARPAD system was developed, based on a custom made adjustable opto-sonovision objective. The core of the system consists of a coaxial adjustable opto-sonovision
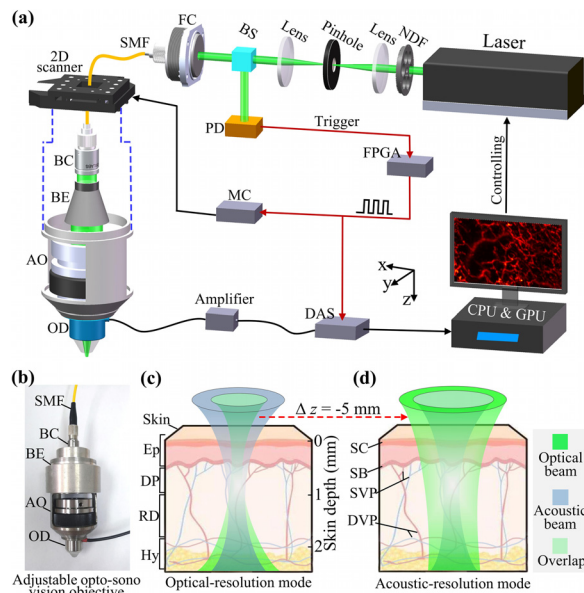
FIG. 1. Schematic of the switchable optical and acoustic resolution photoacoustic dermoscopy (S-OR-ARPAD) system, using an adjustable opto-sonovision objective. (a) Schematic of the entire setup. NDF, neutral density filter; BS, beam splitter; FC, fiber collimator; SMF, single mode fiber; BC, beam collimator; BE, beam expander; AO, adjustable objective; OD, opto-sonodector; PD, photodiode; FPGA, field programmable gate array; MC, machine controller; and DAS, data acquisition system. (b) Photograph of the adjustable opto-sonovision objective with a single-mode fiber. (c) Schematic of optical excitation and photoacoustic (PA) signal generation by multilayered structures of Asiatic skin for OR mode. Ep, epidermis; DP, dermal papillae; RD, reticular dermis; and Hy, hypodermis. (d) Schematic of optical excitation and PA signal generation by multilayered structures of Asiatic skin for AR mode. SC, stratum corneum; SB, stratum basale; SVP, superficial vascular plexus; and DVP, deep vascular plexus.

objective [Fig. 1(b)], which delivers a focused laser pulse and detects the ultrasonic waves resulting from the optical absorption components of skin. A miniature laser (Model DTL-314QT, pulsed Q-switched laser, Russia) operating at 532 nm with a 4 ns pulse width is used as the radiation source. The laser beam is focused by a convex lens (LA1222, Thorlabs, USA), which passes through a 25 μm pinhole for spatial filtering, and then coupled into a single mode fiber using a fiber coupler (PAF-X-7-A, Thorlabs, USA). Finally, the adjustable opto-sonovision objective is used to focus the laser and irradiate the test-area to produce PA signals. Figure 1(b) shows a photograph of the opto-sonovision objective with a single-mode fiber shown in Fig. 1(a), which is mainly composed of a fixed beam collimator (F240FC-532, Thorlabs, USA), a beam expander (BE02–532, Thorlabs, USA), an adjustable objective (working distance of 17 mm and focal depth-adjustable range of 10 mm), and an opto-sonodetector with a central frequency of ∼45 MHz and a bandwidth of 7–83 MHz at −6 dB (supplementary material, Fig. 1). The adjustable objective consists of an Olympus Plan Achromat Objective (RMS4X, Thorlabs, USA) and a custom adjustable casing, which is used to adjust the Olympus Plan Achromat Objective. The adjustable opto-sonovision objective is actuated automatically using a two-dimensional scanner (HRXWJ-50R-2, TianRui ZhongHai, China) when the fast scanning is performed. Around 1% of the pulse energy reflected from a beam splitter in the optical path is collected to monitor the oscillations in the laser pulse power by a photodiode and is also used as a trigger signal to the field programmable gate array (FPGA) system. The FPGA system is used to provide trigger signals to synchronize the acquisition and scanning processes of the entire imaging system. The collected PA signals are sequentially amplified with a 63 dB low noise amplifier (AU-1291, MITEQ, USA), then digitized by a single channel data acquisition card with a 250 MHz sampling frequency (M3i.4121, SPECTRUM, Germany), and finally stored in the computer's hard drive for later imaging reconstruction. To conform to the American National Standards Institute safety limit (20 mJ/cm^2),[43] a neutral density filter (NDF) was used to adjust the fluence density of the laser beam on the tissue surface to 12 mJ/cm^2. All the human experiments followed a protocol approved by the Institutional Review Board administered by the Human Research Protection Office at South China Normal University in Guangzhou.

Furthermore, the scanning head is composed of an adjustable opto-sonovision objective and a two-dimensional scanner, which is flexibly attached to a mechanical arm to control over the relative position between the objective and the skin surface. The position of the adjustable objective can be varied in order to shift the location of the acoustic and optical focuses with respect to the skin surface, so the OR and AR modes of the S-OR-ARPAD can be flexibly switched. For example, if the light illuminating skin surface is focused within the first millimeter from the skin surface, the installation effectively acts as an OR-PAD [Fig. 1(c)]. Conversely, if the light is unfocused, whereas the acoustic focus is located deep inside the skin tissue, the installation turns into an AR-PAD [Fig. 1(d)]. Under the circumstances, by further placing the focus immediately above one another, switchable scanning can be implemented with OR mode achieved in the first millimeter of skin tissue, followed by a slow progression into AR mode in deeper skin tissue layers.

To validate the lateral resolution of the OR and AR modes of the PAD, the experimental measurements of the OR and AR resolutions

were implemented (*Experimental Measurements and Performance Verification*, supplementary material). As shown in Fig. 2 in the supplementary material, the lateral resolutions of the PAD system in OR and AR modes are estimated to be ~4.4 μm and ~47 μm, respectively. In order to measure the axial resolution and imaging depth of the PAD, the experimental measurements of the axial resolution and imaging depth were carried out (*Experimental Measurements and Performance Verification*, supplementary material). As shown in Fig. 3 in the supplementary material, the axial resolution of the PAD is estimated to be ~35 μm. The AR mode of the PAD is able to image the black hair ~1.8 mm beneath the phantom surface with a signal to noise ratio (SNR) of 6 dB compared to only ~1.2 mm by the OR mode of that with the same SNR. Meantime, the lateral resolution of the PAD as a function of the imaging depth is shown in Fig. 4 in the supplementary material. Obviously, as the imaging depth of the PAD increases, the lateral resolution drops sharply for OR mode (imaging depth < 1 mm), but the change in lateral resolution for AR mode is very small (imaging depth > 1 mm). Furthermore, to better understand the performance of PA imaging of skin and optimize the detection characteristics of dermoscopic systems designed for clinical applications, the frequency contributions of different skin layers were identified by two tissue-mimicking phantoms (supplementary material, Fig. 5), which then illustrated that the PAD system employed was appropriate for imaging a large variation of feature sets in skin tissue.

To study how the OR and AR modes of the applied S-OR-ARPAD system depend on different depths, three different skin layers (epidermis, epidermal-dermal junction layer, and vascular network below the epidermal-dermal junction layer) oriented parallel to the skin surface were segmented. With the PAD system, Fig. 2 presents the results obtained in OR and AR modes from the palm skin of one author (*Medical Procedure for Human Skin Imaging*, supplementary material). Figure 2(a) shows the cross-sectional images in OR and AR modes, measuring 5 mm × 1.8 mm, of the palm skin. Figures 2(b)–2(d) show the maximum amplitude projections (MAPs) in the direction perpendicular to skin surface within the depth ranges marked in Fig. 2(a). Notably, the image in AR mode reveals the vessels of the reticular dermis and deep hypodermis not visible in the image by OR mode (white arrows). On the other hand, the higher resolution achieved by OR mode, compared to AR mode, is clearly evident in Figs. 2(b) and 2(c), which depicts the lateral MAPs of the epidermis (0–180 μm below the surface) and the epidermal-dermal junction layer (220–550 μm below the surface). These images reveal the fine details of the skin surface and dermal papillae, with single capillary loops clearly resolved with OR mode but not with AR mode in Fig. 2(c). Figure 2(d) shows the lateral MAPs 460–1800 μm below the skin surface, visualizing the vascular network below the epidermal-dermal junction layer. As evident in Fig. 2(d), the small vessels of the superficial horizontal plexus can be resolved with OR mode, whereas the large vessels of the deeper horizontal plexus are visible with only AR mode, which highlights an example where the improvement of resolution leads to a loss of vascular features. The reason that OR mode cannot resolve the large vessels of the deeper horizontal plexus in Fig. 2(d) is that the depth of the large vessels of the deeper horizontal plexus is beyond the soft-depth limit in human skin (~1 mm).

To investigate the S-OR-ARPAD ability to visualize variations in the skin structure, the optimal PA imaging was performed at the opisthenar and palm areas of the same author by varying the relative
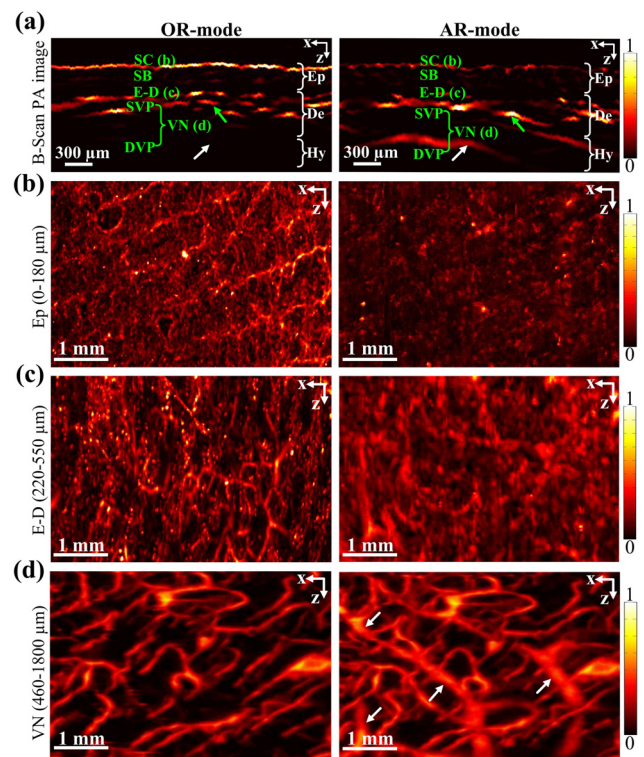
FIG. 2. Comparison of *in vivo* contrasts with OR and AR modes of the S-OR-ARPAD system. (a) Consecutive cross-sectional PA image of the palm area of one author. The arrows (green and white) indicate the vessels of the dermal papillae and reticular dermis and hypodermis, respectively. Ep, epidermis; De, dermis; Hy, hypodermis; SC, stratum corneum; SB, stratum basale; SVP, superficial vascular plexus; DVP, deep vascular plexus; VN, vascular network; and E-D, epidermal-dermal junction layer. (b) Lateral maximum amplitude projections (MAPs) of the epidermis depicting a slice located 0–180 μm below the skin surface. (c) Lateral MAPs of the epidermal-dermal junction layer 220–550 μm below the surface. (d) Lateral MAPs of the vascular network below the epidermal-dermal junction layer at a depth of 460–1800 μm.

position of the acoustic and optical focuses with respect to the skin surface, as shown in Fig. 3. The consecutive cross sections of the PA reconstructed images at these two locations are shown in Fig. 3(a), measuring 5 mm × 1.8 mm. Figures 3(b)–3(d) show the MAPs in the direction perpendicular to the skin surface within the depth ranges marked in Fig. 3(a). As shown in Fig. 3(b), the epidermis of opisthenar and palm skins are located at depth <180 μm, and the epidermis of palm skin can be seen as a skin texture trait with structures as small as 20 μm, and hairs and pores in opisthenar skin can be observed, which shows that the features of the homogeneous skin surface are completely different between opisthenar and palm skins. Figure 3(c) displays the MAPs corresponding to the epidermal-dermal junction layer. As depicted, below the epidermis junction begins the area in which the capillary loops are situated in opisthenar and palm skins. In this layer, small absorbing spots arranged in a stripe pattern can be observed, which are separated by ~0.8 mm and can be seen as single anatomical structures as small as 30 μm located 220–550 μm below the surface in Fig. 3(c). Meantime, the results indicate that the vast vascular networks locate in the lower papillary dermis, morphological structures of which
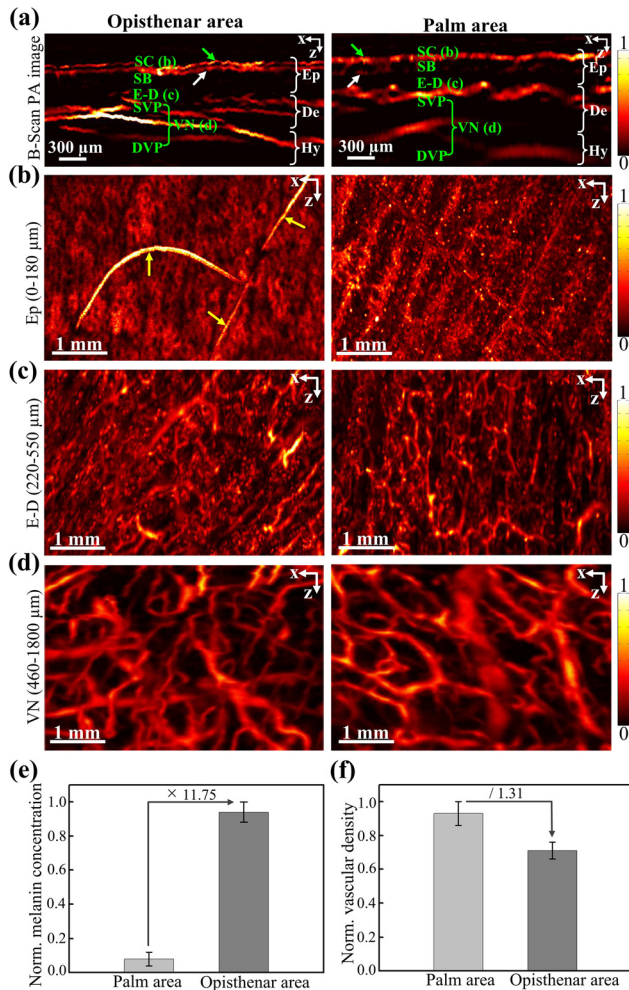
FIG. 3. Comparison of *in vivo* contrasts with opisthenar and palm areas of the same author by the S-OR-ARPAD system. (a) Consecutive cross-sectional PA images of the opisthenar and palm areas. The arrows (green and white) indicate the stratum corneum and the melanin layer in the upper part of stratum basale, respectively. (b) Lateral MAPs of the epidermis depicting a slice located 0–180 μm below the skin surface by OR mode. The yellow arrows indicate fine hairs on the human body. (c) Lateral MAPs of the epidermal-dermal junction layer 220–550 μm below the surface by OR mode. (d) Lateral MAPs of the vascular network below the epidermal-dermal junction layer at a depth of 460–1800 μm by AR mode.

density (*VD*) values were calculated (*Quantitative and Statistical Analyses*, supplementary material), generating two groups of C_M and *VD* values: group 1 from opisthenar skin, whereas group 2 from palm skin. Figures 3(e) and 3(f) show the error bar graph of C_M and *VD* values for the opisthenar and palm skins. As shown in Fig. 3(e), the normalized C_M of the melanin layer of the palm skin (0.082 ± 0.043) is significantly smaller than that of the opisthenar skin (0.943 ± 0.057). Meanwhile, the normalized *VD* below the epidermal-dermal junction layer of opisthenar skin (0.701 ± 0.052) is significantly smaller than that of the palm skin (0.932 ± 0.068) shown in Fig. 3(f). Meantime, the main morphometric parameters of the human skin by repeatedly measuring the opisthenar area of the same author are shown in Table 2 in the supplementary material.

This study presents the qualitative account on the relationship between the OR mode, AR mode, and human skin imaging achieved with S-OR-ARPAD. Here, a design for the PAD with switchable optical and acoustic resolution has been introduced, which can extend the imaging depth of PAD into deep skin tissue layers by the method of a coaxial adjustable opto-sonovision objective with high numerical aperture optical and acoustic focusing. This allows for a smooth transition between OR mode in superficial dermoscopic imaging to AR mode when imaging at greater depths within intensely scattering skin tissues suffering from the degradation of OR performance. The presented coaxial design of light illumination and acoustic detection facilitates the optimal coupling of the excitation light into the imaged skin tissue, thus further enhancing the generated signals and accelerating image acquisition.

Much more work needs to be done, however, before the PAD can be considered for the clinical evaluation of skin diseases. Primarily, the imaging frame rate of 2 B-Scan images per second over an imaging range of 5 mm × 1.8 mm, achieved by the current design, is mainly limited by the performance of the laser source with higher repetition and the fast two-dimensional scanner, which can be generally improved. Additionally, to obtain a greater imaging depth, a longer wavelength irradiation source may be feasible. Finally, the PA blood flow measurement methods should probably be added to the PAD system, which would be more accurate to differentiate the epidermis and dermis of human skin tissue. In conclusion, it is anticipated that the high spatial and temporal resolution of the PAD system, along with its abilities of scalable penetration into scattering skin tissues, will enable important clinical applications, e.g., in the fields of assessment for the visualization of skin abnormalities, vascular diagnostics, and skin cancer research.

See the supplementary material that shows the performance evaluations and imaging method of the S-OR-ARPAD system.

REFERENCES

[1]H. F. Zhang, K. Maslov, G. Stoica, and L. V. Wang, Nat. Biotechnol. **24**, 848–851 (2006).

are obvious differences between opisthenar and palm skins. Below this network of microvasculature of the epidermal-dermal junction layer, the larger vessels that belong to either the lower parts of the superficial vascular plexus or the deep vascular plexus of the dermis and hypodermis can be observed, as shown in Fig. 3(d). The diameters of blood vessels locating 460–1800 μm below the skin surface in Fig. 3(d) range from 30 to 400 μm, and the palm skin has more blood vessels and more complex morphological structures in this layer.

Twenty different regions of skin areas from the same author (each of 5 mm × 3 mm) were randomly selected and examined, 10 from the opisthenar skin and the other 10 from the palm skin. Both the melanin concentration of the melanin layer (C_M) and vascular

[2]L. V. Wang and S. Hu, Science **335**, 1458–1462 (2012).

[3]V. Ntziachristos, Nat. Methods **7**, 603–614 (2010).

[4]X. L. Dean-Ben, G. A. Pang, F. M. de Espinosa, and D. Razansky, Appl. Phys. Lett. **107**, 051105 (2015).

[5]H. Ma, Z. Cheng, Z. Wang, K. Xiong, and S. Yang, Opt. Lett. **44**, 1880–1883 (2019).

[6]W. Zhang, Y. Li, V. P. Nguyen, Z. Huang, Z. Liu, X. Wang, and Y. M. Paulus, Light: Sci. Appl. **7**, 103 (2018).

[7]A. A. Plumb, N. T. Huynh, J. Guggenheim, E. Zhang, and P. Beard, Eur. Radiol. **28**, 1037–1045 (2018).

[8]L. Zeng, G. Liu, D. Yang, and X. Ji, Appl. Phys. Lett. **102**, 053704 (2013).

[9]L. Xi and H. Jiang, Appl. Phys. Lett. **101**, 173702 (2012).

[10]F. Gao, X. Feng, and Y. J. Zheng, Appl. Phys. Lett. **104**, 213701 (2014).

[11]H. Ma, S. Yang, Z. Cheng, and D. Xing, Opt. Lett. **42**, 2342–2345 (2017).

[12]H. Ma, Z. Cheng, Z. Wang, Y. Gu, T. Zhang, H. Qiu, and S. Yang, Appl. Phys. Lett. **113**, 083704 (2018).

[13]Y. Wang, D. Xu, S. Yang, and D. Xing, Biomed. Opt. Express **7**, 279–286 (2016).

[14]J. Y. Sim, C.-G. Ahn, E.-J. Jeong, and B. K. Kim, Sci. Rep. **8**, 1059 (2018).

[15]H. Ma, K. Xiong, J. Wu, X. Ji, and S. Yang, Appl. Phys. Lett. **114**, 133701 (2019).

[16]M. Schwarz, D. Soliman, M. Omar, A. Buehler, S. V. Ovsepian, J. Aguirre, and V. Ntziachristos, IEEE Trans. Med. Imaging **36**, 1287–1296 (2017).

[17]J. Sun, Q. Zhou, and S. Yang, Opt. Express **26**, 4967–4978 (2018).

[18]M. Schwarz, M. Omar, A. Buehler, J. Aguirre, and V. Ntziachris, IEEE Trans. Med. Imaging **34**, 672–677 (2015).

[19]Y. Matsumoto, Y. Asao, H. Sekiguchi, A. Yoshikawa, T. Ishii, K.-I. Nagae, S. Kobayashi, I. Tsuge, S. Saito, M. Takada, Y. Ishida, M. Kataoka, T. Sakurai, T. Yagi, K. Kabashima, S. Suzuki, K. Togash, T. Shiina, and M. Toi, Sci. Rep. **8**, 14930 (2018).

[20]C. Huang, K. Wang, L. M. Nie, L. H. V. Wang, and M. A. Anastasio, IEEE Trans. Med. Imaging **32**, 1097–1110 (2013).

[21]C. Song, L. Xi, and H. Jiang, Opt. Lett. **38**, 2930–2933 (2013).

[22]S. Vaithilingam, T. J. Ma, Y. Furukawa, I. O. Wygant, X. Zhuang, A. D. L. Zerda, and B. T. Khuri-yakub, IEEE Trans. Ultrason. Ferroelectr. Freq. Control **56**, 2411–2419 (2009).

[23]I. N. Papadopoulos, O. Simandoux, S. Farahi, J. P. Huignard, E. Bossy, D. Psaltis, and C. Moser, Appl. Phys. Lett. **102**, 211106 (2013).

[24]J. Yao and L. V. Wang, Photoacoustics **2**, 87–101 (2014).

[25]B. Judkewitz, Y. M. Wang, R. Horstmeyer, A. Mathy, and C. Yang, Nat. Photonics **7**, 300–305 (2013).

[26]B. Cox and B. Treeby, IEEE Trans. Med. Imaging **29**, 387–396 (2010).

[27]Z. Xie, W. Roberts, P. Carson, X. Liu, C. Tao, and X. Wang, Opt. Lett. **36**, 4815–4817 (2011).

[28]S. Han, C. Lee, S. Kim, M. Jeon, J. Kim, and C. Kim, Appl. Phys. Lett. **103**, 203702 (2013).

[29]W. Qin, W. Qi, T. Jin, H. Guo, and L. Xi, Appl. Phys. Lett. **111**, 263704 (2017).

[30]H. F. Zhang, K. Maslov, and M. Sivaramakrishnan, Appl. Phys. Lett. **90**, 053901 (2007).

[31]J. Yang, J. Li, S. He, and L. V. Wang, Optica **6**, 250–256 (2019).

[32]J. Yang, L. Li, A. A. Shemetov, S. Lee, Y. Zhao, Y. Liu, Y. Shen, J. Li, Y. Oka, V. V. Verkhusha, and L. V. Wang, Sci. Adv. **5**, eaay1211 (2019).

[33]P. Beard, Interface Focus **1**, 602 (2011).

[34]R. G. Maev, *Acoustic Microscopy: Fundamentals and Applications* (WileyVCH Verlag GmbH & Co. Weinheim, 2008).

[35]E. W. Stein, K. Maslov, and L. V. Wang, J. Appl. Phys. **105**, 102027 (2009).

[36]L.-D. Liao, C.-T. Lin, Y.-Y. I. Shih, T. Q. Duong, H.-Y. Lai, P.-H. Wang, R. Wu, S. Tsang, J.-Y. Chang, M.-L. Li, and Y.-Y. Chen, J. Cereb. Blood Flow Metab. **32**, 938–951 (2012).

[37]W. Xing, L. Wang, K. Maslov, and L. V. Wang, Opt. Lett. **38**, 52–54 (2013).

[38]S. Jeon, J. Kim, and C. Kim, Proc. SPIE **9708**, 970845 (2016).

[39]M. Moothanchery and M. Pramanik, Sensors **17**, 357 (2017).

[40]H. Estrada, J. Turner, M. Kneipp, and D. Razansky, Laser Phys. Lett. **11**, 045601 (2014).

[41]H. He, G. Wissmeyer, S. V. Ovsepian, A. Buehler, and V. Ntziachristos, Opt. Lett. **41**, 2708–2710 (2016).

[42]Z. Guo, Y. Li, and S.-L. Chen, Opt. Lett. **43**, 1119–1122 (2018).

[43]American National Standards Institute and The Laser Institute of America, *American National Standard for Safe Use of Lasers* (The Laser Institute of America, Orlando, FL, USA, 2014).